Enhancement of high-order harmonic generation in graphene by mid-infrared and terahertz fields

Wenwen Mao [1], Angel Rubio [1,2] and Shunsuke A. Sato [3,1,*]

[1]*Max Planck Institute for the Structure and Dynamics of Matter and Center for Free-Electron Laser Science, 22761 Hamburg, Germany*
[2]*Center for Computational Quantum Physics, Flatiron Institute, New York, New York 10010, USA*
[3]*Center for Computational Sciences, University of Tsukuba, Tsukuba 305-8577, Japan*

We theoretically investigate high-order harmonic generation (HHG) in graphene under mid-infrared (MIR) and terahertz (THz) fields based on a quantum master equation. Numerical simulations show that MIR-induced HHG in graphene can be enhanced by a factor of 10 for fifth harmonic and a factor of 25 for seventh harmonic under a THz field with a peak strength of 0.5 MV/cm by optimizing the relative angle between the MIR and THz fields. To identify the origin of this enhancement, we compare the fully dynamical calculations with a simple thermodynamic model and a nonequilibrium population model. The analysis shows that the enhancement of the high-order harmonics mainly results from a coherent coupling between MIR- and THz-induced transitions that goes beyond a simple THz-induced population contribution.

I. INTRODUCTION

Recent developments in laser technologies have enabled the generation of intense light [1–3], opening an avenue into the investigation of light-matter interactions in nonlinear regimes. High-order harmonic generation (HHG) is an extremely nonlinear optical phenomenon involving extreme photon upconversion. This phenomenon was first observed in atomic gases [4,5]. A semiclassical three-step model has provided a clear understanding of gas-phase HHG [6,7]. Gas-phase HHG has been utilized to generate ultrashort attosecond light pulses [2] for investigating light-induced ultrafast electron dynamics in atoms [8–10], molecules [11–13], and solids [14–17]. HHG from a solid-state system was first observed in 2011 [18] and has recently been attracting considerable interest from both fundamental and technological points of view [19–23].

Among various materials, the HHG from graphene has been intensively investigated theoretically. It has been suggested that HHG can be efficiently induced in graphene because of the unique electronic structure of this material, specifically the Dirac cone [24–27]. Recently, HHG from graphene has been experimentally observed in the mid-infrared (MIR) [28,29] and terahertz (THz) [30,31] regimes, exhibiting unique ellipticity dependence and high efficiency. We previously investigated HHG from graphene in both the MIR and THz regimes based on a quantum master equation [32,33]. In the MIR regime, coupling between field-induced intraband and interband transitions opens important channels for HHG, enhancing HHG with finite ellipticity [32]. A real-time electron dynamics simulation in the THz regime has shown that it is essential to consider the nonequilibrium steady state resulting from the balance between field-driving and relaxation to go beyond the equilibrium thermodynamic picture of HHG from graphene [33].

It is important to improve the efficiency of solid-state HHG to develop novel HHG-based light sources and spectroscopies. In recent studies, it has been suggested that HHG from graphene can be enhanced using two-color laser fields based on various mechanisms [34–36]. In Ref. [34], the two-color HHG is suggested with the combination of the electron-hole pair creation by high-frequency pump light and the acceleration of the created pairs by low-frequency light. Mrudul *et al.* investigated the HHG from graphene with bicircular fields, controlling the valley polarization [35]. Furthermore, Avetissian *et al.* investigated the HHG from graphene with a linearly polarized light and its second harmonics, showing that when the two-color fields are perpendicularly polarized, the stronger harmonics can be emitted compared with the parallel polarization [36].

In this study, we explore the possibility of using a THz field to enhance MIR-induced HHG in graphene based on the knowledge gained from previous studies. First we use a quantum master equation to compute the electron dynamics under MIR and THz fields and evaluate the emitted harmonic spectra. We compare the results of the fully dynamical calculations with a thermodynamic model considering the equilibrium Fermi-Dirac distribution and with a nonequilibrium population model considering a population distribution in a nonequilibrium steady state. As a result of the analysis, we find that coupling via the induced coherence by THz and

*ssato@ccs.tsukuba.ac.jp

MIR fields plays an essential role in enhancing MIR-induced HHG, clarifying the importance of the field-induced coherence beyond the simple population effect.

The paper is organized as follows. In Sec. II, we briefly describe the theoretical method for describing electron dynamics in graphene induced by MIR and THz fields. In Sec. III, we investigate the impact of a THz field on MIR-induced HHG from graphene and explore the microscopic mechanism of the enhancement by employing the thermodynamic model and the nonequilibrium population model. Finally, our findings are summarized in Sec. IV.

II. METHODS

A. Electron dynamics calculation based on a quantum master equation

Here we briefly describe theoretical methods for computing light-induced electron dynamics in graphene and how the calculated dynamics can be used to analyze HHG. These methods have been described in detail in previous works [33,37,38].

In this study, we use the following quantum master equation to describe electron dynamics in graphene:

$$\frac{d}{dt}\rho_k(t) = \frac{1}{i\hbar}[H_{k+eA(t)/\hbar}, \rho_k(t)] + \hat{D}[\rho_k(t)], \quad (1)$$

where $\rho_k(t)$ is the one-body reduced density matrix for the Bloch wave vector k and $H_{k+eA(t)/\hbar}$ is the one-body Hamiltonian. Here light-matter coupling is described by an additional term in the Hamiltonian, a spatially uniform vector potential $A(t)$, which is related to the applied electric field as $A(t) = -\int_{-\infty}^{t} dt' E(t')$, in the long-wavelength approximation. The relaxation operator is denoted as $\hat{D}[\rho_k(t)]$. Based on the previous studies [33,37], we employ the relaxation-time approximation [39] for the relaxation operator in the Houston basis expression [40,41]. Those Houston states $|u_{bk}^H(t)\rangle$ are simply the instantaneous eigenstates of the time-dependent Hamiltonian and satisfy the following instantaneous eigenvalue problem:

$$H_{k+eA(t)/\hbar}|u_{bk}^H(t)\rangle = \epsilon_{b,k+eA(t)/\hbar}|u_{bk}^H(t)\rangle, \quad (2)$$

where b denotes the band index and $\epsilon_{b,k+eA(t)/\hbar}$ are the instantaneous eigenvalues of the Hamiltonian. The reduced density matrix can be expanded in the Houston states as

$$\rho_k(t) = \sum_{bb'} \rho_{bb',k}(t)|u_{bk}^H(t)\rangle\langle u_{b'k}^H(t)|, \quad (3)$$

where $\rho_{bb',k}(t)$ are the expansion coefficients.

We introduce the relaxation operator $\hat{D}[\rho_k(t)]$ with the following Houston basis expression [37,38] as

$$\hat{D}[\rho_k(t)] = -\sum_b \frac{\rho_{bb,k}(t) - f^{FD}\big(\epsilon_{b,k+eA(t)/\hbar}, T_e, \mu\big)}{T_1}$$
$$\times |u_{bk}^H(t)\rangle\langle u_{bk}^H(t)| - \sum_{b\neq b'} \frac{\rho_{bb',k}(t)}{T_2}|u_{bk}^H(t)\rangle\langle u_{b'k}^H(t)|. \quad (4)$$

From Refs. [33,37], the longitudinal relaxation time T_1 is set to 100 fs, and the transverse relaxation time T_2 is set

to 20 fs. Here $f^{FD}(\epsilon, T_e, \mu) = \frac{1}{e^{(\epsilon-\mu)/k_BT_e}+1}$ is the Fermi-Dirac distribution, in which we set the electron temperature T_e to 300 K and the chemical potential μ to 0, unless stated otherwise. We confirmed that the choice of the relaxation times, T_1 and T_2, does not affect the qualitative results and conclusions that will be presented in the later part of the paper (see Appendix A).

We describe the electronic structure of graphene employing a tight-binding Hamiltonian in the atomic orbital basis representation with nearest-neighbor hopping [42] as follows:

$$H_k = \begin{bmatrix} 0 & t_0 f(k) \\ t_0 f(k)^* & 0 \end{bmatrix}, \quad (5)$$

where t_0 is the nearest-neighbor hopping and $f(k)$ is given by $f(k) = e^{ik\cdot\delta_1} + e^{ik\cdot\delta_2} + e^{ik\cdot\delta_3}$ with the nearest-neighbor vector δ_j. According to Ref. [42], the nearest-neighbor hopping t_0 is set to 2.8 eV, and the lattice constant a is set to 1.42 Å.

To describe electron dynamics, we directly solve the quantum master equation, Eq. (1), in the time domain by employing the Runge-Kutta method. Since we do not apply any approximation to solve the equation of motion, field-induced modifications of electronic structures, such as the Stark effect, Rabi splitting [43], and the band-gap opening at the Dirac point [44], are naturally described even under dissipation [45].

By using the time-dependent density matrix $\rho_k(t)$ evolved with Eq. (1), the total energy of the electronic system can be evaluated as

$$E_{tot}(t) = \frac{2}{\Omega_{BZ}}\int dk \text{Tr}[H_{k+eA(t)/\hbar}\rho_k(t)], \quad (6)$$

where Ω_{BZ} is the volume of the first Brillouin zone.

Similarly, the electric current density is given by

$$J(t) = \frac{2}{(2\pi)^2}\int dk \text{Tr}[\hat{J}_k(t)\rho_k(t)], \quad (7)$$

where the current operator $\hat{J}_k(t)$ is defined as

$$\hat{J}_k(t) = -\frac{e}{m_e\hbar}\frac{\partial H_{k+eA(t)/\hbar}}{\partial k}. \quad (8)$$

The current density $J(t)$ induced by an intense electric field $E(t)$ is analyzed to investigate HHG. For example, the power spectrum of the emitted harmonics can be evaluated by applying the Fourier transform to the current density $J(t)$ as follows:

$$I_{HHG}(\omega) \sim \omega^2 \left|\int_{-\infty}^{\infty} dt J(t) e^{i\omega t}\right|^2. \quad (9)$$

III. RESULTS

A. MIR-induced HHG in graphene under THz fields and the quasistatic approximation

We first analyze the HHG induced by a MIR laser pulse in the presence of THz fields. For practical calculations, we employ the following form for the MIR pulse:

$$A_{MIR}(t) = -\frac{E_{MIR}}{\omega_{MIR}}e_{MIR}\sin(\omega_{MIR}t)\cos^4\left(\frac{\pi}{T_{MIR}}t\right) \quad (10)$$

in the domain $-T_{MIR}/2 < t < T_{MIR}/2$ and zero outside this domain. Here E_{MIR} is the peak strength of the MIR field,
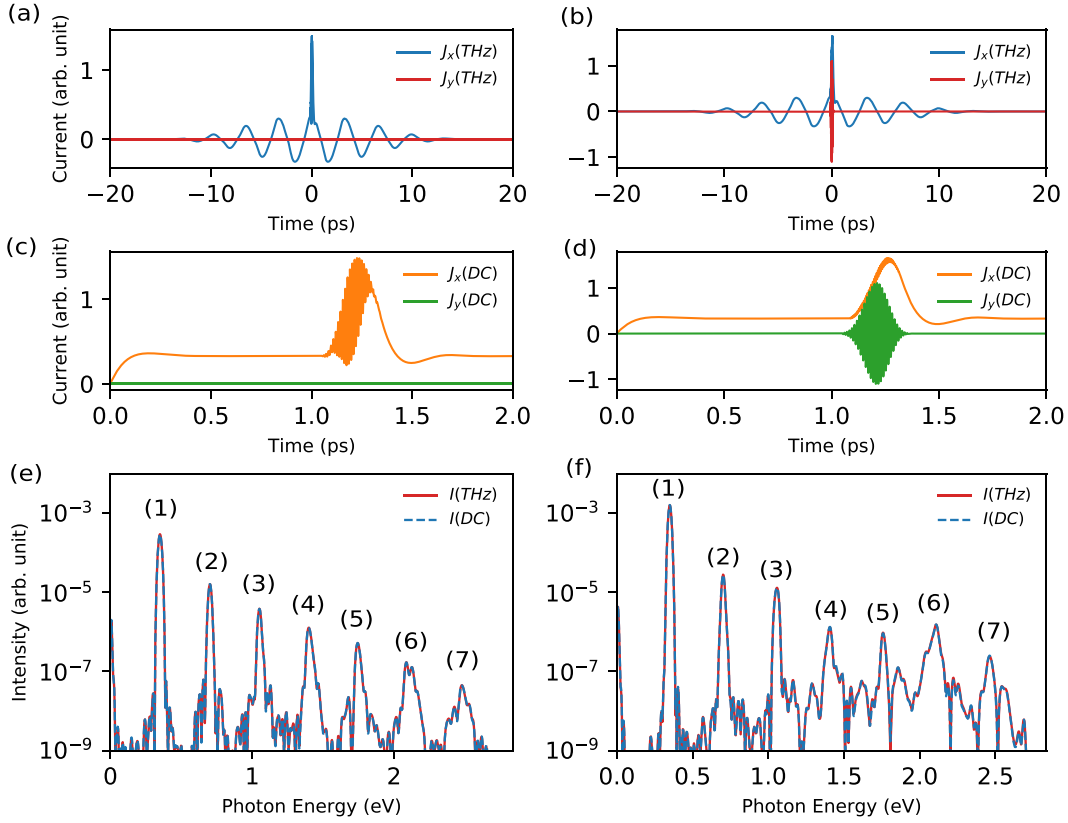
FIG. 1. [(a) and (b)] The current $\boldsymbol{J}(t)$ induced by THz and MIR fields, $\boldsymbol{E}_{\text{THz}}(t) + \boldsymbol{E}_{\text{MIR}}(t)$. The x component of the current is shown as the blue line, whereas the y component is shown as the red line. (a) The time profile of the applied THz field. [(c) and (d)] The current $\boldsymbol{J}(t)$ induced by the static and MIR fields, $\boldsymbol{E}_{\text{dc}}(t) + \boldsymbol{E}_{\text{MIR}}(t - \tau_{\text{MIR}})$. The x component of the current is shown as the orange line, whereas the y component is shown as the green line. In (a) and (c), the polarization of all the fields is parallel to the Γ-M direction (the x direction in the present setup) as $\boldsymbol{e}_{\text{THz}} = \boldsymbol{e}_{\text{dc}} = \boldsymbol{e}_{\text{MIR}} = \boldsymbol{e}_x$. In (b) and (d), the polarization of THz and static fields is parallel to the x direction as $\boldsymbol{e}_{\text{THz}} = \boldsymbol{e}_{\text{dc}} = \boldsymbol{e}_{\text{MIR}} = \boldsymbol{e}_x$, while that of the MIR field is perpendicular as $\boldsymbol{e}_{\text{MIR}} = \boldsymbol{e}_y$. (e) The power spectra $I_{\text{HHG}}(\omega)$ computed using the current in (a) and (c). (f) The power spectra $I_{\text{HHG}}(\omega)$ computed using the current in (b) and (d).

ω_{MIR} is the mean frequency, $\boldsymbol{e}_{\text{MIR}}$ is a unit vector along the polarization direction of light, and T_{MIR} is the pulse duration. In this study, the pulse duration T_{MIR} is set to 0.4 ps, and the mean frequency ω_{MIR} is set to $0.35424\,\text{eV}/\hbar$. We compute the electron dynamics by changing the other parameters.

Similarly, we employ the following form for the THz pulse:

$$A_{\text{THz}}(t) = -\frac{E_{\text{THz}}}{\omega_{\text{THz}}} \boldsymbol{e}_{\text{THz}} \sin(\omega_{\text{THz}}t) \cos^4\left(\frac{\pi}{T_{\text{THz}}}t\right) \qquad (11)$$

in the domain $-T_{\text{THz}}/2 < t < T_{\text{THz}}/2$ and zero outside this domain. Here E_{THz} is the peak strength of the THz field, ω_{THz} is the mean frequency, $\boldsymbol{e}_{\text{THz}}$ is a unit vector along the polarization direction, and T_{THz} is the pulse duration. In this study, the pulse duration T_{THz} is set to 40 ps and the mean frequency ω_{THz} is set to $1.2407\,\text{meV}/\hbar$. The time profile of the applied THz electric field is shown in the inset of Fig. 1(a).

To gain insight into THz-assisted MIR-induced HHG in graphene, we perform the electron dynamics calculation in the presence of both THz and MIR fields, $\boldsymbol{E}_{\text{THz}}(t) + \boldsymbol{E}_{\text{MIR}}(t)$. Here we set E_{MIR} to 6.5 MV/cm and E_{THz} to 0.5 MV/cm. We note that intense THz pulses with amplitudes exceeding 1 MV/cm are available experimentally [46]. The polarization direction of the THz field $\boldsymbol{e}_{\text{THz}}$ is set to the Γ-M direction (the x direction in our setup), whereas the polarization direc-

tion of the MIR field $\boldsymbol{e}_{\text{MIR}}$ is treated as a tunable parameter. Figures 1(a) and 1(b) show the computed current $\boldsymbol{J}(t)$ induced by $\boldsymbol{E}_{\text{THz}}(t) + \boldsymbol{E}_{\text{MIR}}(t)$ as a function of time. The result with the parallel configuration ($\boldsymbol{e}_{\text{MIR}} = \boldsymbol{e}_x = \boldsymbol{e}_{\text{THz}}$) is shown in Fig. 1(a), while the result with the perpendicular configuration ($\boldsymbol{e}_{\text{MIR}} = \boldsymbol{e}_y \perp \boldsymbol{e}_{\text{THz}}$) is shown in Fig. 1(b). The x and y components are shown as blue and red lines, respectively. As seen from Figs. 1(a) and 1(b), the THz field induces a current on the picosecond timescale, whereas the MIR field induces a current on a much shorter timescale.

We analyze MIR-induced HHG by extracting the current induced by the MIR field in the presence of the THz field. We define two kinds of currents for this purpose. The first current is induced by both the THz and MIR fields and is denoted as $\boldsymbol{J}^{\text{THz+MIR}}(t)$. The second current is induced solely by the THz field and is denoted as $\boldsymbol{J}^{\text{THz}}(t)$. We define the current induced by the MIR field in the presence of the THz field as $\boldsymbol{J}^{\text{eff}}(t) = \boldsymbol{J}^{\text{THz+MIR}}(t) - \boldsymbol{J}^{\text{THz}}(t)$. The Fourier transform is applied to the extracted current $\boldsymbol{J}^{\text{eff}}(t)$, and the power spectrum of the emitted harmonics is computed using Eq. (9). The solid line in Fig. 1(e) shows the power spectrum computed using the current $\boldsymbol{J}(t)$ presented in Fig. 1(a), where the polarization directions of the THz and MIR fields are parallel, and the solid line in Fig. 1(f) shows the power spectrum

computed using the current $\boldsymbol{J}(t)$ presented in Fig. 1(b), where the polarization directions of the two fields are perpendicular. Figure 1(e) shows that second and higher even-order harmonics are generated in addition to odd-order harmonics because the THz field breaks the inversion symmetry of the system locally in time. This second-harmonic generation is known as electric-field-induced second-harmonic generation or THz-induced second-harmonic generation [47–50]. Even-order harmonics are similarly generated in the perpendicular configuration ($\boldsymbol{e}_{\mathrm{MIR}} \perp \boldsymbol{e}_{\mathrm{THz}}$), as can be seen from Fig. 1(f).

Explicit use of the THz pulse in the electron dynamics calculation increases the propagation time (42 ps in the present case), as can be seen Figs. 1(a) and 1(b). Hence, the electron dynamics calculation with the explicit inclusion of THz pulses has a large computational cost. To reduce the computational cost of modeling MIR-induced HHG in graphene in the presence of a THz field, we replace the THz pulse with a static field based on the quasistatic approximation [33]. For practical analysis, we perform two simulations. In the first simulation, the electron dynamics are calculated under a static field $\boldsymbol{E}_{\mathrm{dc}}(t) = \boldsymbol{e}_{\mathrm{dc}}E_{\mathrm{dc}}\Theta(t)$ that is suddenly switched on at $t = 0$. Here $\boldsymbol{e}_{\mathrm{dc}}$ is the unit vector along the polarization direction of the static field, and E_{dc} is the field strength. Immediately after the static field is switched on, the driven electron dynamics induce a current. The driven system reaches a steady state after a sufficiently long time propagation time, and the current becomes constant in time. We denote the current induced solely by $\boldsymbol{E}_{\mathrm{dc}}(t)$ as $\boldsymbol{J}^{\mathrm{dc}}(t)$. In the second simulation, the electron dynamics are calculated under both MIR and static fields, $\boldsymbol{E}_{\mathrm{dc}}(t) + \boldsymbol{E}_{\mathrm{MIR}}(t - \tau_{\mathrm{MIR}})$, where the pulse center of the MIR field is shifted by τ_{MIR}. We denote the current induced by $\boldsymbol{E}_{\mathrm{dc}}(t) + \boldsymbol{E}_{\mathrm{MIR}}(t - \tau_{\mathrm{MIR}})$ as $\boldsymbol{J}^{\mathrm{dc+MIR}}(t)$. The shift τ_{MIR} can be made sufficiently large time to investigate the MIR-induced electron dynamics for a full nonequilibrium steady state realized by the static field $\boldsymbol{E}_{\mathrm{dc}}(t)$. The MIR-induced current can be extracted as $\boldsymbol{J}^{\mathrm{eff}}(t) = \boldsymbol{J}^{\mathrm{dc+MIR}}(t) - \boldsymbol{J}^{\mathrm{dc}}(t)$ to analyze MIR-induced HHG in the presence of the static field.

Figures 1(c) and 1(d) show the current $\boldsymbol{J}^{\mathrm{dc+MIR}}(t)$ induced by both static and MIR fields. The x and y components of the current are shown as orange and green lines, respectively. Here the static field is polarized along the Γ-M direction (the x direction in our setup), and the field strength E_{dc} is the same as the peak strength of the THz field, $E_{\mathrm{dc}} = E_{\mathrm{THz}} = 0.5$ MV/cm. The MIR field used in Fig. 1(c) is the same as that used in Fig. 1(a) and has a polarization direction parallel to that of the static field. By contrast, the MIR field used in Fig. 1(d) is the same as that used in Fig. 1(b) and has a polarization direction perpendicular to that of the static field. To apply the MIR field to the nonequilibrium steady state under the static field, we set the time delay τ_{MIR} of the MIR field to 1 ps, which is sufficiently longer than the relaxation timescales of the quantum master equation, T_1 and T_2.

To analyze HHG in the presence of the static field $\boldsymbol{E}_{\mathrm{dc}}(t)$, we extract the current $\boldsymbol{J}^{\mathrm{eff}}(t)$ induced by the MIR field in the presence of the static field by subtracting $\boldsymbol{J}^{\mathrm{dc}}(t)$ from $\boldsymbol{J}^{\mathrm{dc+MIR}}(t)$: $\boldsymbol{J}^{\mathrm{eff}}(t) = \boldsymbol{J}^{\mathrm{dc+MIR}}(t) - \boldsymbol{J}^{\mathrm{dc}}(t)$. The dashed lines in Figs. 1(e) and 1(f) correspond to the HHG spectra computed using the current shown in Figs. 1(c) and 1(d), respectively. The results of the quasistatic approximation with a static field are identical to those computed by explicitly including the

THz pulse. Therefore, the quasistatic approximation is valid for analyzing HHG under MIR and THz fields. We further confirmed the validity of the quasistatic approximation for different static field strengths (see Appendix B). Hereafter, we employ the static field within the quasistatic approximation instead of explicitly including the THz pulse. The agreement between results obtained using the quasistatic approximation and the explicit inclusion of the THz pulse indicates that the nonequilibrium steady state under the static field plays an important role in MIR-induced HHG in graphene in the presence of a THz field.

B. Orientational dependence of HHG

Here we investigate HHG in graphene within the quasistatic approximation by changing the relative angle between the static and MIR fields. For practical analysis, the direction of the static field $\boldsymbol{e}_{\mathrm{dc}}$ is fixed to the Γ-M axis (the x axis in our setup), and the peak field strength of the MIR field E_{MIR} is fixed at 6.5 MV/cm. The emitted harmonics are investigated by manipulating the polarization direction of the MIR field, $\boldsymbol{e}_{\mathrm{MIR}}$, and the strength of the static field, E_{dc}.

To analyze the HHG efficiency, we compute the signal intensity of the emitted harmonics at each order by integrating the power spectrum within a finite energy range as follows:

$$I_{\mathrm{total}}^{n\mathrm{th}} = \int_{(n-\frac{1}{2})\omega_{\mathrm{MIR}}}^{(n+\frac{1}{2})\omega_{\mathrm{MIR}}} d\omega I_{\mathrm{HHG}}(\omega). \tag{12}$$

Here $I_{\mathrm{total}}^{n\mathrm{th}}$ is the integrated intensity of the emitted nth harmonic.

Figures 2(a)–2(d) show the computed angular dependence of the emitted harmonic yield $I^{n\mathrm{th}}$ for different harmonic orders. The angle θ denotes the relative angle between the MIR and static fields. In Fig. 2(a), there is no second harmonic generation in the absence of a static field because graphene has intrinsic inversion symmetry. By contrast, the second harmonics are generated under the application of a static field because of the breakdown of the inversion symmetry. For a static field strength of 0.5 MV/cm, the emitted second-harmonic intensity is maximized at a relative angle of approximately 45°.

In Fig. 2(b), the third-harmonic yield is almost isotropic (black line) in the absence of a static field, reflecting the rotational symmetry of the Dirac cone (see also Appendix C). By contrast, the third-harmonic intensity exhibits a strong angular dependence under the application of a strong static field ($E_{\mathrm{dc}} = 1.0$ MV/cm): The third-harmonic emission is considerably enhanced when the static and MIR fields are perpendicular to each other, while it is suppressed when these two fields are parallel. The enhancement of the third harmonic for the perpendicular configuration can be understood in terms of the coupling between the intraband transition induced by the static field and the interband transition induced by the MIR field, as suggested in the previous study [32].

The higher-order harmonics exhibit a more complex angular dependence under a static field, as shown in Figs. 2(c) and 2(d). In particular, the fifth-order harmonic emission can be considerably enhanced in the presence of static or THz fields [Fig. 2(d)]. For example, the intensity of the fifth-order
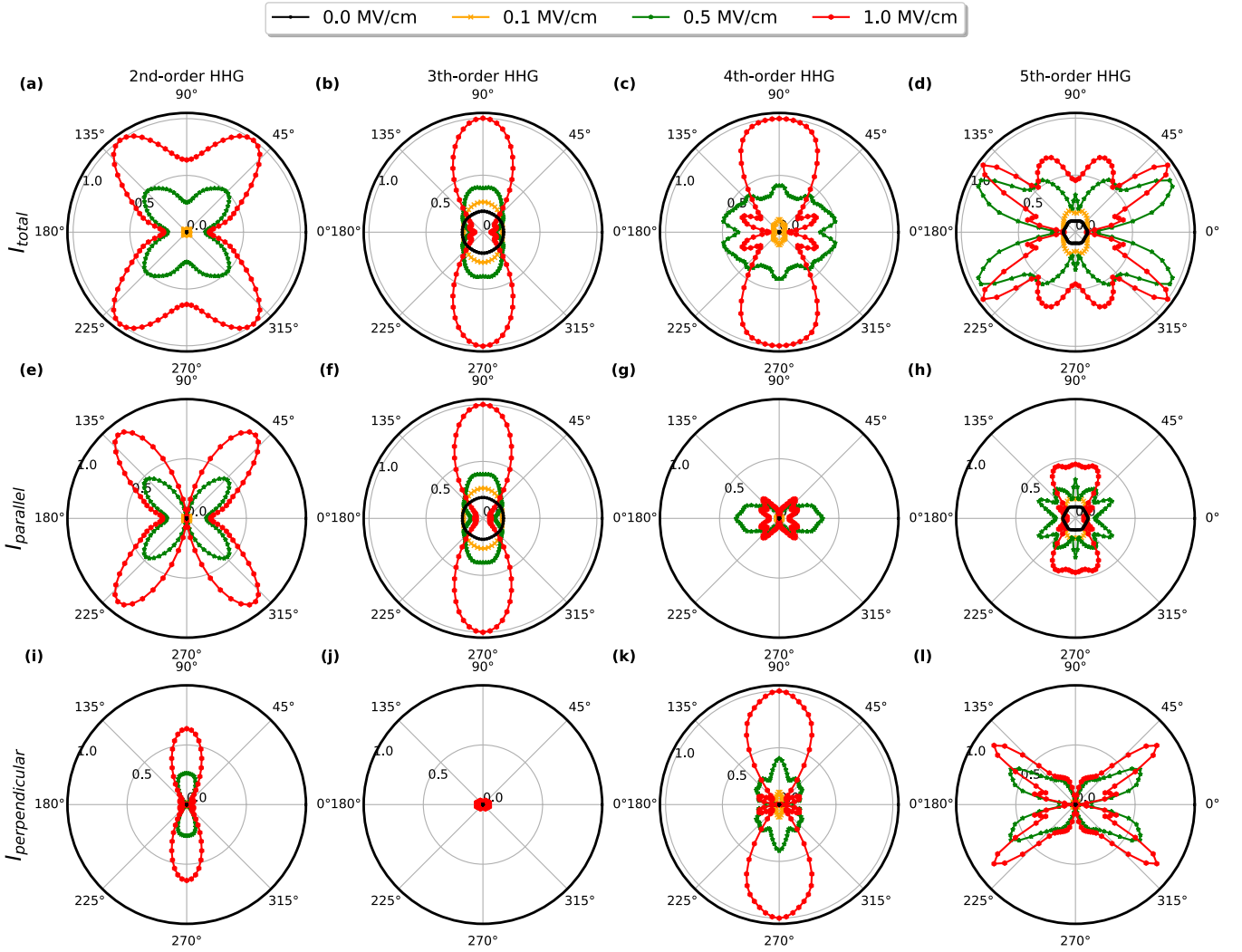
FIG. 2. The angular dependence of the harmonic yield in the nonequilibrium steady states under a static field along the Γ-M direction is shown for different static field strengths, E_{dc}. The angle θ denotes the relative angle between the static field and the MIR field. [(a)–(d)] The total intensity I_{total}^{nth} is shown for the second, third, fourth, and fifth harmonics. [(e)–(h)] The component of the intensity parallel to $\boldsymbol{e}_{MIR}$ is shown for each harmonic. [(i)–(l)] The component of the intensity perpendicular to $\boldsymbol{e}_{MIR}$ is shown for each harmonic. The results are normalized by the maximum total intensity I_{total}^{nth} for each harmonic.

harmonic is enhanced more than 10 times by applying a static field with a strength of 0.5 MV/cm with respect to the result solely induced by the MIR field [see the green line in Fig. 2(d)]. This enhancement ratio is larger than that of the third-order harmonic. Hence, a larger field-induced enhancement is expected for higher-order harmonics. In fact, the seventh-order harmonic is enhanced 25 times when the static field strength is 0.5 MV/cm (see Appendix D).

To further elucidate the angular dependence of HHG in graphene, we decompose the harmonic intensity $I_{HHG}(\omega)$ into parallel and perpendicular components with respect to the polarization of the driving MIR field. The parallel component of the HHG intensity is defined as

$$I_{HHG}^{para}(\omega) \sim \omega^2 \left| \int_{-\infty}^{\infty} dt \, \boldsymbol{e}_{MIR} \cdot \boldsymbol{J}(t) e^{i\omega t} \right|^2, \qquad (13)$$

where $\boldsymbol{e}_{MIR}$ is the unit vector along the polarization direction of the MIR field. Likewise, the perpendicular component is

defined as

$$I_{HHG}^{perp}(\omega) \sim \omega^2 \left| \int_{-\infty}^{\infty} dt \, \bar{\boldsymbol{e}}_{MIR} \cdot \boldsymbol{J}(t) e^{i\omega t} \right|^2, \qquad (14)$$

where $\bar{\boldsymbol{e}}_{MIR}$ is a unit vector perpendicular to $\boldsymbol{e}_{MIR}$, i.e., $\bar{\boldsymbol{e}}_{MIR} \cdot \boldsymbol{e}_{MIR} = 0$. The total intensity I_{HHG} in Eq. (9) is reproduced by the sum of $I_{HHG}^{para}(\omega)$ and $I_{HHG}^{perp}(\omega)$ as $I_{HHG}(\omega) = I_{HHG}^{para}(\omega) + I_{HHG}^{perp}(\omega)$.

Equations (13) and (14) are employed to decompose the emitted harmonic intensity into parallel and perpendicular components. Figures 2(e)–2(h) and 2(i)–2(l) show the angular dependence of the parallel and perpendicular components the harmonic intensity for orders, respectively.

In Figs. 2(a), 2(e) and 2(i), the parallel component of the second harmonic under the static field reaches a maximum at approximately 45° and dominates the total second-harmonic intensity at this angle. By contrast, the maximum perpendicular component is always obtained when the MIR and static fields are perpendicular to each other. In Figs. 2(b),

2(f) and 2(j), the third harmonic is dominated by the parallel component for any angle and static field strength over the investigated range. For both second- and third-harmonic generation, the parallel components are dominant when the emitted harmonic intensity is maximized.

There are qualitative differences between the lower-order harmonics (the second- and third-order harmonics) and the higher-order harmonics (the fourth- and fifth-order harmonics). In Fig. 2(c), the fourth harmonic yield reaches a maximum at an angle θ of 90° under the strongest applied static field, $E_{dc} = 1.0$ MV/cm. A comparison of Figs. 2(g) and 2(k) shows that the perpendicular component dominates the emitted harmonic intensity in this case. As seen from Figs. 2(d), 2(h), and 2(l), the emitted fifth harmonic at the most efficient angle is dominated by the perpendicular component, in spite of the fact that the parallel component is dominant at all angles in the absence of a static field. Hence, the emission paths of the perpendicular components are expected to be important for the enhancement of MIR-induced HHG by a THz field. We observe the same trend for higher-order harmonics (see Appendix D).

C. Comparison of the nonequilibrium steady state and the thermodynamic model

Here we investigate the role of a nonequilibrium steady state in HHG by comparing the results of the quasistatic approximation with those of the thermodynamic model [51], which has been employed to investigate the HHG in graphene in the THz regime [30,31]. As introduced in Sec. III A, the quasistatic approximation consists of replacing the THz pulse with the corresponding static field to describe the electronic system under a THz field. By contrast, the thermodynamic model consists of approximating the electronic system under a THz pulse by a thermal state with a high electron temperature [51]. The difference between the quasistatic approximation and the thermodynamic model reflects the difference between the nonequilibrium and equilibrium distributions, clarifying the role of the nonequilibrium steady state in HHG.

The quasistatic approximation is characterized by the strength of the static field, E_{dc}, whereas the thermodynamic model is characterized by the electron temperature T_e. To compare these two models that are formulated using different parameters, we introduce the excess energy [33] as a common measure of the excitation intensity. The excess energy corresponding to the quasistatic approximation is computed as the change in the total energy given in Eq. (6) of the nonequilibrium steady state caused by the application of the static field $E_{dc}(t)$. Hence, the excess energy of the nonequilibrium steady state depends on the static field strength as $\Delta E_{excess}^{non-eq}(E_{dc})$. The excess energy of the thermodynamic model is computed as the change in the total energy caused by increasing the temperature from room temperature ($T_e = 300$ K) and hence depends on the electron temperature as $\Delta E_{excess}^{thermo}(T_e)$. Thus, converting both the static field strength E_{dc} in the quasistatic approximation and the electron temperature T_e in the thermodynamic model to common excess energy enables the two models to be objectively and quantitatively compared [33].

Figure 3 shows the comparison of the results obtained using quasistatic approximation and the thermodynamic model.
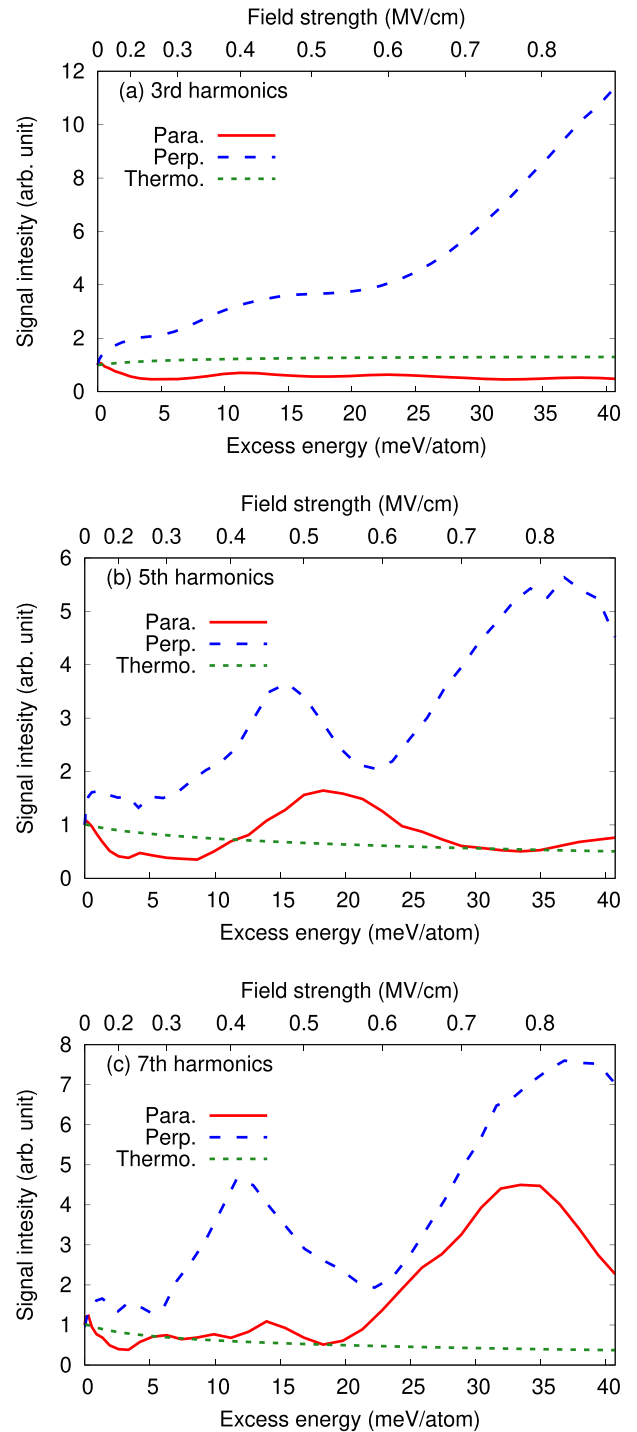

FIG. 3. The emitted light intensity, $I^{n\text{th}}$, is shown as a function of the excess energy for (a) third (b) fifth, and (c) seventh harmonics. The results for the nonequilibrium steady states induced by a static field parallel (red solid line) and perpendicular (blue dashed line) to the MIR field are compared with the thermodynamic model (green dotted line). In each panel, the field strength of the static field parallel to the MIR field is shown as the secondary axis.

The MIR field strength is set to 6.5 MV/cm, and the MIR field polarization direction is set to the Γ-M direction (the x axis of the present setup). The thermodynamic model preserves the intrinsic inversion symmetry of graphene and therefore

does not produce even-order harmonics. Hence, we only analyze the odd-order harmonics generated by this model. Figure 3(a) shows that the MIR-induced third harmonic within the quasistatic approximation is considerably enhanced and suppressed for parallel and perpendicular configurations, respectively. By contrast, the result within the thermodynamic model remains almost constant. Figures 3(b) and 3(c) show that the fifth- and seventh-harmonic yields are significantly enhanced under a static field within the quasistatic approximation, while those harmonic yields decrease slightly as the electron temperature increases within the thermodynamic model. Hence, the enhancement of HHG cannot be described by simple heating of electronic systems within the thermodynamic model and originates from the nonequilibrium nature of field-induced electronic dynamics. The small change in the harmonic yields within the thermodynamic model relative to that predicted by the nonequilibrium steady-state picture indicates that modification of the population distribution around the Fermi level has little effect on the spectra of HHG.

D. Contribution of the nonequilibrium population

Having demonstrated the importance of the nonequilibrium steady state under a THz field, we elucidate the role of a *coherent* coupling between the MIR and THz fields beyond the simple population contribution induced by the THz field. To highlight the coherent coupling contribution, we evaluate the contribution from *incoherent* coupling by introducing a nonequilibrium population distribution model as an extension of the thermodynamic model. Within the thermodynamic model, the contribution from the THz field is described by modifying the population distribution by increasing the electronic temperature of the reference Fermi-Dirac distribution. Hence, the thermodynamic population only captures the population contribution (the diagonal element of the density matrix) of the THz-induced effect based on the thermal distribution. Here we extend the thermodynamic model by replacing the reference Fermi-Dirac distribution in the relaxation operator in Eq. (4) with the population distribution of the nonequilibrium steady state under a static field. The extended model includes the population contribution (given by diagonal elements of the density matrix), but it does not include THz-induced coherence (given by the off-diagonal elements of the density matrix). Hence, a comparison of the nonequilibrium population model and the fully dynamical model can reveal the contribution from the coherent coupling between the THz and MIR fields.

To formulate the nonequilibrium population model, we first analyze the population distribution in the nonequilibrium steady state under a static field. The population distribution in the Brillouin zone can be expressed as

$$n_{b\mathbf{k}}(t) = \int d\mathbf{k}' \delta[\mathbf{k} - \mathbf{K}'(t)] \mathrm{Tr}\big[\big|u_{b\mathbf{k}'}^H(t)\big\rangle\big\langle u_{b\mathbf{k}'}^H(t)\big|\rho_{\mathbf{k}'}(t)\big]$$
$$= \big\langle u_{b,\mathbf{k}-e\mathbf{A}(t)}^H(t)\big|\rho_{\mathbf{k}-e\mathbf{A}(t)}(t)\big|u_{b,\mathbf{k}-e\mathbf{A}(t)}^H(t)\big\rangle, \quad (15)$$

where $\mathbf{K}'(t)$ is the accelerated wave vector in accordance with the acceleration theorem, $\mathbf{K}'(t) = \mathbf{k}' + e\mathbf{A}(t)$. The population distribution in the nonequilibrium steady state can be evaluated in the long-time propagation limit under a static
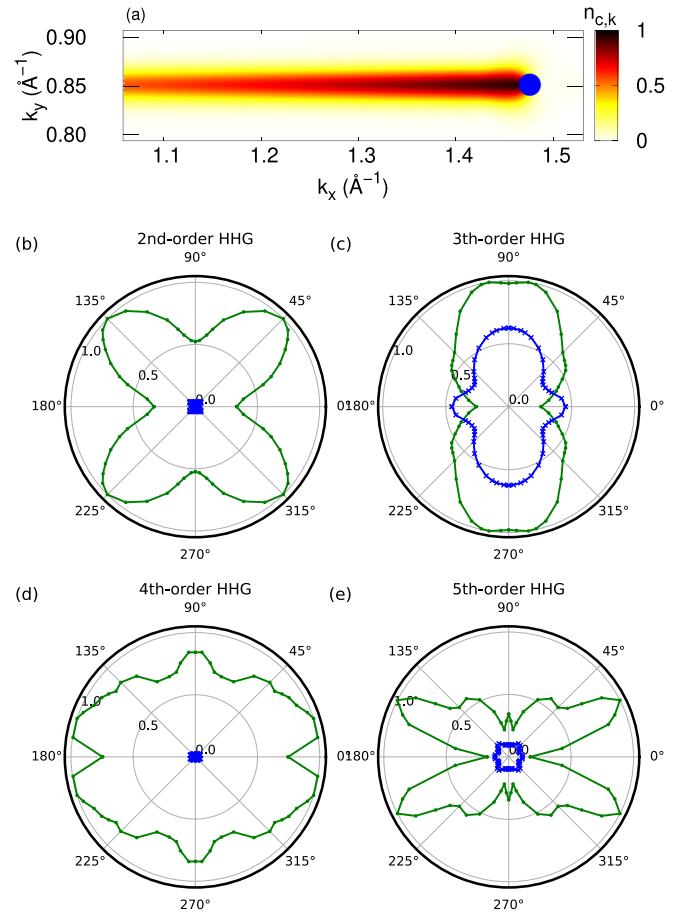

FIG. 4. (a) The calculated conduction population distribution, $n_{c\mathbf{k}}^{\mathrm{neq-steady}}$ for the nonequilibrium steady state is shown. Here the Dirac point is indicated by the blue circle. [(b)–(e)] The angular dependence of the emitted harmonic intensity is shown for the (b) second, (c) third, (d) fourth, and (e) fifth harmonics. The results obtained using the nonequilibrium population model and the nonequilibrium steady state are shown by the blue and green solid lines, respectively.

field $\mathbf{A}(t) = -\mathbf{E}_{\mathrm{dc}}t$,

$$n_{b\mathbf{k}}^{\mathrm{neq-steady}} = \lim_{t \to \infty} n_{b\mathbf{k}}(t). \quad (16)$$

Figure 4(a) shows the population distribution in the conduction band for the nonequilibrium steady state under a static field with a strength of $E_{\mathrm{dc}} = 0.5$ MV/cm. The static field is polarized along the Γ-M direction (x axis). The Dirac point (K point) is depicted by the blue circle. In Fig. 4(a), the region to the left of the Dirac point is largely occupied by the field-induced population in the nonequilibrium steady state, whereas the region to the right of the Dirac point is almost empty, breaking the inversion symmetry of the system. We employ this nonequilibrium population distribution as the reference distribution of the relaxation operator in Eq. (4) instead of the Fermi-Dirac distribution to construct the nonequilibrium population model.

Figure 4(b) shows the angular dependence of the second-harmonic yield in the presence of a static field with a strength of $E_{\mathrm{dc}} = 0.5$ MV/cm. The corresponding angular

dependencies of the third, fourth, and fifth harmonics are shown in Figs. 4(c)–4(e), respectively. In each panel, the results obtained using the nonequilibrium population model are shown as the blue solid line, and the results obtained using the quasistatic approximation are shown as the green solid line, which is identical to the result shown in Fig. 2. In Figs. 4(b) and 4(d), the even-order harmonics computed with the nonequilibrium population model are negligibly weak compared with those computed using the fully dynamical calculation based on the quasistatic approximation. This result indicates that under the charge-neutral condition ($\mu = 0$) investigated here, the two- and four-photon resonances of the MIR field are far from the Fermi level and cannot be modified by the population changes around the Fermi surface, resulting in small contributions to even-order harmonic generations. By contrast, within the fully dynamic calculation, the THz field can coherently couple with the MIR field via the off-diagonal elements of the density matrix. Thus, the coherent coupling can be realized both around the Fermi level and anywhere in the Brillouin zone, as long as the dipole transition is allowed. Hence, the coherent coupling contribution may enhance the contribution from the resonant quantum pass, inducing stronger even-order harmonic generation.

Figure 4(c) shows that the third-harmonic yield calculated using the fully dynamical model is 1.57 times stronger than that computed using the nonequilibrium population model when the two fields are perpendicular. This result indicates that the THz field enhances third-harmonic generation for the perpendicular configuration and that both coherent coupling and the incoherent population play important roles in the THz-assisted enhancement mechanism. By contrast, the third-harmonic yield computed using the fully dynamical calculation is 0.57 times smaller than that computed using the nonequilibrium population model when the two fields are parallel. This result indicates that the contributions from the coherent coupling and the incoherent population cancel each other, weakening the total signal. Therefore, both coherent coupling and incoherent population affect third-harmonic generation under the investigated condition but play different roles depending on the relative angle θ between the THz and MIR fields.

Figure 4(e) shows that the fifth-order harmonic yield computed using the fully dynamical calculation is considerably larger than that computed using the nonequilibrium population model, except in the range where the THz and MIR fields are parallel. Hence, the coherent coupling is the dominant contribution to the enhancement of fifth-harmonic generation for most angles but the effects of coherent coupling and the incoherent population are both important when the MIR and THz fields are parallel. The consistent results are obtained for higher-order harmonics (see Appendix D). When a MIR field is solely applied to graphene, the induced HHG can be attributed to the interference between multiple excitation pathways involving nonlinear coupling between MIR-induced intraband and interband transitions [32]. In contrast, the substantial enhancement of HHG observed in the presence of THz fields suggests the activation of an additional nonlinear coupling mechanism. This mechanism, which arises through coherent coupling between MIR- and THz-induced

transitions, appears to predominate over other processes in contributing to the overall harmonic yield.

IV. SUMMARY

We used a quantum master equation to model MIR-induced HHG in graphene in the presence of a strong THz field. We first computed the electron dynamics in graphene by explicitly employing MIR and THz pulses and evaluated the emitted high-harmonic spectra. Next, we developed a quasistatic approximation by analyzing MIR-induced HHG under a static field to replace the THz pulses. The THz-assisted MIR-induced HHG spectra were accurately reproduced by a static field within the quasistatic approximation, thus validating the application of this approximation for describing the induced dynamics generated by an applied strong THz field.

We then investigated the intensity of the emitted harmonics for different relative angles between the MIR and THz fields. In the absence of a THz field, the emitted odd-order harmonics exhibit an almost circular angular dependence, reflecting the circular symmetry of Dirac cones, whereas no even-order harmonics are emitted because of the intrinsic inversion symmetry of graphene. Under an intense THz field, the emitted harmonics exhibit a strong angular dependence along with enhancement and suppression of the harmonic yield. For example, the emitted fifth harmonic can be enhanced 10 times under a THz field with a strength of 0.5 MV/cm with respect to the result without the THz field, as shown in Fig. 2(d).

To elucidate the mechanism by which a THz field enhances MIR-induced HHG, we compared the results obtained using the quasistatic approximation and the thermodynamic model, which treats the effect of the THz field as a simple increase in the electron temperature of the Fermi-Dirac model [51]. The thermodynamic model does not reproduce the enhancement of MIR-induced HHG, indicating that nonequilibrium THz-induced dynamics play an essential role in the enhancement.

To gain further insight into the enhancement of MIR-induced HHG by a THz field, we developed a nonequilibrium population distribution model. Within this model, THz-induced effects are treated as a change in the population distribution in the nonequilibrium steady state. The results obtained using the fully dynamical calculation and the nonequilibrium population distribution model were compared to elucidate the roles of coherent coupling between the MIR and THz fields. The THz-induced even-order harmonics and the THz-enhanced high-order harmonics are dominated by the coherent coupling contribution, whereas the enhancement of the third harmonics under a THz field is affected by both the coherent coupling and the nonequilibrium population. Furthermore, the enhancement of the higher-order harmonics is dominated by the coherent coupling contribution. These enhancement mechanisms are not rigidly limited by the conditions of the laser parameters investigated in this work but can be induced in rather general conditions. Therefore, it is key to control both the coherent coupling and the population for enhancing HHG from solids by employing multicolor laser fields. Moreover, the coherent coupling mechanism holds pivotal significance across various orders of harmonic generation, including low-order harmonic phenomena (see Fig. 4). This implies the indispensability of field-induced coherence
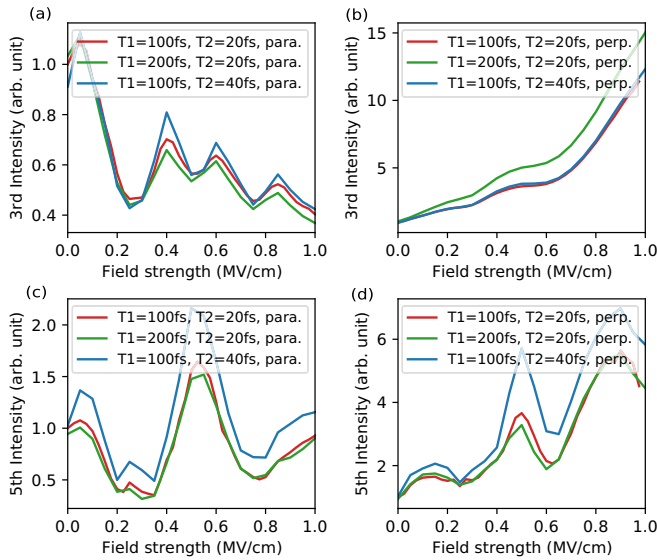
FIG. 5. The harmonic yields are shown as a function of the static field strength E_{dc}. In each panel, the results obtained using the different relaxation times, T_1 and T_2, are compared. The results of the third harmonics are shown in (a) and (b), whereas those of the fifth harmonics are shown in (c) and (d). The results obtained using the parallel configuration ($\boldsymbol{e}_{MIR} = \boldsymbol{e}_x = \boldsymbol{e}_{THz}$) are shown in (a) and (c), whereas those obtained using the perpendicular configuration ($\boldsymbol{e}_{MIR} = \boldsymbol{e}_y \perp \boldsymbol{e}_{THz}$) are shown in (b) and (d).

FIG. 6. The power spectra of emitted harmonics, $I_{HHG}(\omega)$, are shown. The results obtained using a weak THz field ($E_{THz} = 0.1$ MV/cm) are shown in (a) and (b), while those obtained using a strong THz field ($E_{THz} = 1.0$ MV/cm) are shown in (c) and (d). The results obtained using the parallel configuration ($\boldsymbol{e}_{MIR} = \boldsymbol{e}_x = \boldsymbol{e}_{THz}$) are shown in (a) and (c), whereas those obtained using the perpendicular configuration ($\boldsymbol{e}_{MIR} = \boldsymbol{e}_y \perp \boldsymbol{e}_{THz}$) are shown in (b) and (d).

in general nonlinear optical effects. Consequently, these findings suggest the prospect of efficient control of electron and spin dynamics through coherent coupling, utilizing multicolor lasers. This capability would extend beyond mere frequency conversion of light, paving the way toward the development of ultrafast optoelectronics and optospintronics.

APPENDIX A: RELAXATION-TIME, T_1 AND T_2, DEPENDENCE

Here we explore the effect of the relaxation times, T_1 and T_2, on the HHG in the presence of THz and MIR fields. Employing the methods described in Sec. II, we calculate the third- and fifth-order harmonic yields with different relaxation times. The results are shown in Fig. 5. The computed results
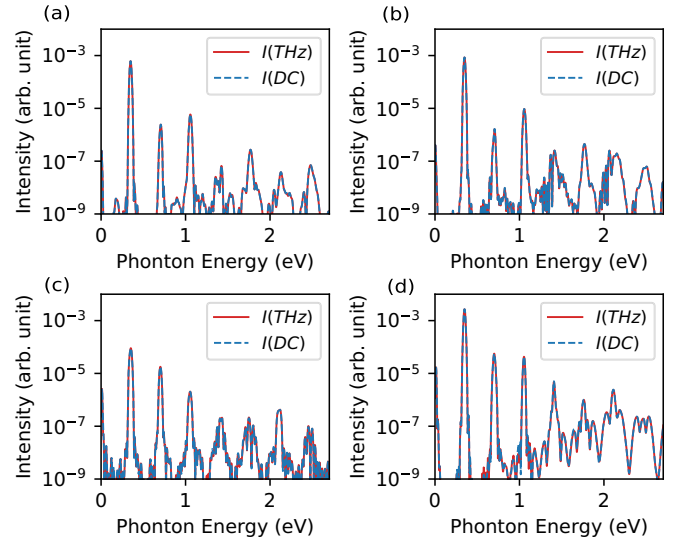
demonstrate that the qualitative trends in the enhancement of the HHG by the THz field irradiation remain consistent for different relaxation times. Hence, the choice of the relaxation times does not have a significant impact on the enhancement.

The relaxation time is determined by various scattering mechanisms including electron-electron scattering, electron-phonon scattering, and electron-impurity scattering. Hence, the actual relaxation times in a realistic setup depends on the experimental conditions. Nevertheless, the results shown in Fig. 5 indicates that the enhancement of the HHG by the THz field irradiation can be realized as a robust phenomenon in a wide range of the experimental conditions.

APPENDIX B: QUASISTATIC APPROXIMATION WITH DIFFERENT THZ FIELD STRENGTHS

Here we extend our investigation to establish the validity of the quasistatic approximation for different THz field strength. Here we repeated the analysis of Figs. 1(e) and 1(f) by changing the THz field strength. The results obtained using a weak THz field ($E_{THz} = 0.1$ MV/cm) are shown in in Figs. 6(a) and 6(b), whereas those obtained using a strong THz field ($E_{THz} = 1.0$ MV/cm) are shown in Figs. 6(c) and 6(d). As seen from the figure, the results of the quasistatic approximation accurately reproduce those of the calculations with the THz laser pulses for all the investigated field strengths and polarization directions. Hence, we confirm that the quasistatic approximation can well describe the electron dynamics in graphene under THz and MIR fields in both the weak- and the strong-field regimes.
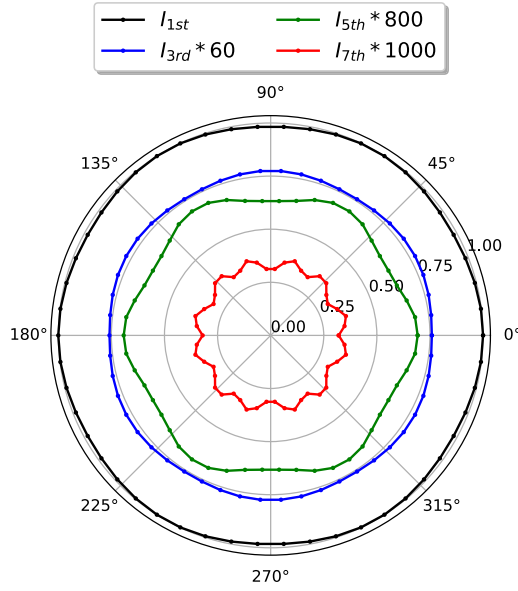
FIG. 7. The angular dependence of the harmonic yield obtained from the electron dynamics calculations in the presence of the MIR field. The numerical conditions are the same as those of the calculations in Fig. 2. The third, fifth, and seventh harmonic yields are scaled by factors of 60, 800, and 1000, respectively.

APPENDIX C: ANGULAR DEPENDENCE OF HIGH-ORDER HARMONIC GENERATION WITHOUT THZ FIELDS

Here we evaluate the angular dependence of the emitted harmonic yield $I^{n\text{th}}$ without THz fields, analyzing the intrinsic symmetry of graphene. Figure 7 show the computed angular dependence of the emitted harmonic yield $I^{n\text{th}}$ obtained using only the MIR field in the same conditions as Fig. 2. Reflecting the sixfold symmetry of the hexagonal lattice of graphene, the emitted harmonics also show the sixfold symmetry in the angular dependence. As seen from Fig. 7, the lower-order harmonics exhibit an almost circular angular dependence, reflecting the circular symmetry of Dirac cones. By contrast, the higher-order harmonics exhibit more complex sixfold symmetry in the angular dependence since electronic structure of graphene deviates from a simple Dirac cone when a single-particle energy is far from the Dirac point.

APPENDIX D: ANGULAR DEPENDENCE OF HIGH-ORDER HARMONICS

Here we analyze the angular dependence of the high-order harmonics in the same way as that used to analyze Fig. 2. Figures 8(a) and 8(b) show the angular dependence of the sixth and seventh harmonics, respectively. Figures 8(c) and 8(e) show the sixth-harmonic signal decomposed into parallel and perpendicular components, respectively. The same decomposition is shown for the seventh-order harmonic in Figs. 8(d) and 8(f).

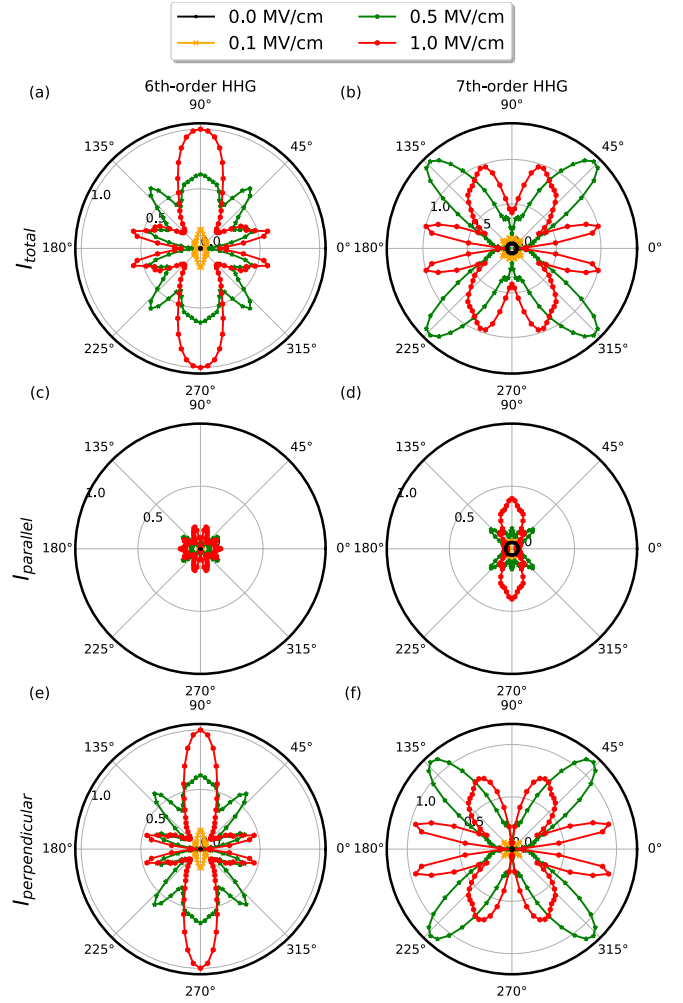Consistent with the results for the fourth and fifth harmonics shown in Fig. 2, the perpendicular components make a

FIG. 8. The angular dependence of the harmonic yields in the nonequilibrium steady state under a static field along the Γ-M direction is shown. The angle θ denotes the relative angle between the static field and the MIR field. [(a) and (b)] The total intensity $I_{\text{total}}^{n\text{th}}$ for the sixth and seventh harmonics is shown, respectively. [(c) and (d)] The component of the intensity parallel to $\boldsymbol{e}_{\text{MIR}}$ is shown for each harmonic. [(e) and (h)] Th component of the intensity perpendicular to $\boldsymbol{e}_{\text{MIR}}$ is shown for each harmonic. The results are normalized by the maximum total intensity $I_{\text{total}}^{n\text{th}}$ of each harmonic.
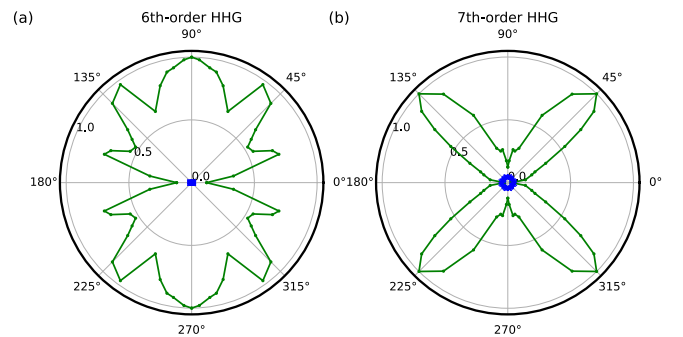

FIG. 9. The angular dependence of the emitted harmonic intensity for the (a) sixth and (b) seventh harmonics are shown. The results obtained using the nonequilibrium population model and the nonequilibrium steady state are shown by the blue and green solid lines, respectively.

large contribution to the enhancement of MIR-induced HHG by a THz field, as shown in Fig. 8.

Furthermore, we compare the results for the sixth and seventh harmonics obtained using the nonequilibrium population model and the nonequilibrium steady state. Figures 9(a) and 9(b) show the angular dependence of the sixth- and seventh-harmonic yields in the presence of a static field with a strength of $E_{dc} = 0.5$ MV/cm, respectively

Consistent with the analysis results shown in Fig. 4, the coherent coupling between the MIR and THz fields plays an essential role in the enhancement of the HHG and goes beyond the simple field-induced population contribution.

---

[1] T. Brabec and F. Krausz, Rev. Mod. Phys. **72**, 545 (2000).

[2] F. Krausz and M. Ivanov, Rev. Mod. Phys. **81**, 163 (2009).

[3] G. Mourou, N. Fisch, V. Malkin, Z. Toroker, E. Khazanov, A. Sergeev, T. Tajima, and B. Le Garrec, Opt. Commun. **285**, 720 (2012).

[4] A. McPherson, G. Gibson, H. Jara, U. Johann, T. S. Luk, I. A. McIntyre, K. Boyer, and C. K. Rhodes, J. Opt. Soc. Am. B **4**, 595 (1987).

[5] M. Ferray, A. L'Huillier, X. F. Li, L. A. Lompre, G. Mainfray, and C. Manus, J. Phys. B: At., Mol. Opt. Phys. **21**, L31 (1988).

[6] P. B. Corkum, Phys. Rev. Lett. **71**, 1994 (1993).

[7] M. Lewenstein, P. Balcou, M. Y. Ivanov, A. L'Huillier, and P. B. Corkum, Phys. Rev. A **49**, 2117 (1994).

[8] E. Goulielmakis, Z.-H. Loh, A. Wirth, R. Santra, N. Rohringer, V. S. Yakovlev, S. Zherebtsov, T. Pfeifer, A. M. Azzeer, M. F. Kling, S. R. Leone, and F. Krausz, Nature (Lond.) **466**, 739 (2010).

[9] H. Wang, M. Chini, S. Chen, C.-H. Zhang, F. He, Y. Cheng, Y. Wu, U. Thumm, and Z. Chang, Phys. Rev. Lett. **105**, 143002 (2010).

[10] M. Holler, F. Schapper, L. Gallmann, and U. Keller, Phys. Rev. Lett. **106**, 123601 (2011).

[11] E. R. Warrick, W. Cao, D. M. Neumark, and S. R. Leone, J. Phys. Chem. A **120**, 3165 (2016).

[12] M. Reduzzi, W.-C. Chu, C. Feng, A. Dubrouil, J. Hummert, F. Calegari, F. Frassetto, L. Poletto, O. Kornilov, M. Nisoli, C.-D. Lin, and G. Sansone, J. Phys. B: At., Mol. Opt. Phys. **49**, 065102 (2016).

[13] N. Saito, N. Douguet, H. Sannohe, N. Ishii, T. Kanai, Y. Wu, A. Chew, S. Han, B. I. Schneider, J. Olsen, L. Argenti, Z. Chang, and J. Itatani, Phys. Rev. Res. **3**, 043222 (2021).

[14] M. Schultze, K. Ramasesha, C. Pemmaraju, S. Sato, D. Whitmore, A. Gandman, J. S. Prell, L. J. Borja, D. Prendergast, K. Yabana, D. M. Neumark, and S. R. Leone, Science **346**, 1348 (2014).

[15] M. Lucchini, S. A. Sato, A. Ludwig, J. Herrmann, M. Volkov, L. Kasmi, Y. Shinohara, K. Yabana, L. Gallmann, and U. Keller, Science **353**, 916 (2016).

[16] H. Mashiko, K. Oguri, T. Yamaguchi, A. Suda, and H. Gotoh, Nat. Phys. **12**, 741 (2016).

[17] F. Siegrist, J. A. Gessner, M. Ossiander, C. Denker, Y.-P. Chang, M. C. Schröder, A. Guggenmos, Y. Cui, J. Walowski, U. Martens, J. K. Dewhurst, U. Kleineberg, M. Münzenberg, S. Sharma, and M. Schultze, Nature (Lond.) **571**, 240 (2019).

[18] S. Ghimire, A. D. DiChiara, E. Sistrunk, P. Agostini, L. F. DiMauro, and D. A. Reis, Nat. Phys. **7**, 138 (2011).

[19] S. Ghimire and D. A. Reis, Nat. Phys. **15**, 10 (2019).

[20] R. E. F. Silva, Á. Jiménez-Galán, B. Amorim, O. Smirnova, and M. Ivanov, Nat. Photon. **13**, 849 (2019).

[21] K. Nakagawa, H. Hirori, S. A. Sato, H. Tahara, F. Sekiguchi, G. Yumoto, M. Saruyama, R. Sato, T. Teranishi, and Y. Kanemitsu, Nat. Phys. **18**, 874 (2022).

[22] A. Gorlach, M. E. Tzur, M. Birk, M. Krüger, N. Rivera, O. Cohen, and I. Kaminer, High-harmonic generation driven by quantum light, Nature Phys. **19**, 1689 (2023).

[23] O. Neufeld, N. Tancogne-Dejean, H. Hübener, U. D. Giovannini, and A. Rubio, Are there universal signatures of topological phases in high harmonic generation? probably not, (2023) arXiv:2303.17300 [cond-mat.mtrl-sci].

[24] S. A. Mikhailov, Europhys. Lett. **79**, 27002 (2007).

[25] K. L. Ishikawa, Phys. Rev. B **82**, 201402(R) (2010).

[26] I. Al-Naib, J. E. Sipe, and M. M. Dignam, Phys. Rev. B **90**, 245423 (2014).

[27] P. Bowlan, E. Martinez-Moreno, K. Reimann, T. Elsaesser, and M. Woerner, Phys. Rev. B **89**, 041408(R) (2014).

[28] N. Yoshikawa, T. Tamaya, and K. Tanaka, Science **356**, 736 (2017).

[29] S. Cha, M. Kim, Y. Kim, S. Choi, S. Kang, H. Kim, S. Yoon, G. Moon, T. Kim, Y. W. Lee *et al.*, Nat. Commun. **13**, 6630 (2022).

[30] H. A. Hafez, S. Kovalev, J.-C. Deinert, Z. Mics, B. Green, N. Awari, M. Chen, S. Germanskiy, U. Lehnert, J. Teichert, Z. Wang, K.-J. Tielrooij, Z. Liu, Z. Chen, A. Narita, K. Müllen, M. Bonn, M. Gensch, and D. Turchinovich, Nature (Lond.) **561**, 507 (2018).

[31] S. Kovalev, H. A. Hafez, K.-J. Tielrooij, J.-C. Deinert, I. Ilyakov, N. Awari, D. Alcaraz, K. Soundarapandian, D. Saleta, S. Germanskiy, M. Chen, M. Bawatna, B. Green, F. H. L. Koppens, M. Mittendorff, M. Bonn, M. Gensch, and D. Turchinovich, Sci. Adv. **7**, eabf9809 (2021).

[32] S. A. Sato, H. Hirori, Y. Sanari, Y. Kanemitsu, and A. Rubio, Phys. Rev. B **103**, L041408 (2021).

[33] W. Mao, A. Rubio, and S. A. Sato, Phys. Rev. B **106**, 024313 (2022).

[34] H. K. Avetissian, A. K. Avetissian, B. R. Avchyan, and G. F. Mkrtchian, Phys. Rev. B **100**, 035434 (2019).

[35] M. S. Mrudul, Álvaro Jiménez-Galán, M. Ivanov, and G. Dixit, Optica **8**, 422 (2021).

[36] H. K. Avetissian, G. F. Mkrtchian, and A. Knorr, Phys. Rev. B **105**, 195405 (2022).

[37] S. A. Sato, J. W. McIver, M. Nuske, P. Tang, G. Jotzu, B. Schulte, H. Hübener, U. De Giovannini, L. Mathey, M. A. Sentef, A. Cavalleri, and A. Rubio, Phys. Rev. B **99**, 214302 (2019).

[38] S. A. Sato, P. Tang, M. A. Sentef, U. D. Giovannini, H. Hübener, and A. Rubio, New J. Phys. **21**, 093005 (2019).

[39] T. Meier, G. von Plessen, P. Thomas, and S. W. Koch, Phys. Rev. Lett. **73**, 902 (1994).

[40] W. V. Houston, Phys. Rev. **57**, 184 (1940).

[41] J. B. Krieger and G. J. Iafrate, Phys. Rev. B **33**, 5494 (1986).

[42] A. H. Castro Neto, F. Guinea, N. M. R. Peres, K. S. Novoselov, and A. K. Geim, Rev. Mod. Phys. **81**, 109 (2009).

[43] R. Merlin, Am. J. Phys. **89**, 26 (2021).

[44] T. Oka and H. Aoki, Phys. Rev. B **79**, 081406(R) (2009).

[45] S. A. Sato, U. D. Giovannini, S. Aeschlimann, I. Gierz, H. Hübener, and A. Rubio, J. Phys. B: At., Mol. Opt. Phys. **53**, 225601 (2020).

[46] H. Hirori, A. Doi, F. Blanchard, and K. Tanaka, Appl. Phys. Lett. **98**, 091106 (2011).

[47] R. W. Terhune, P. D. Maker, and C. M. Savage, Phys. Rev. Lett. **8**, 404 (1962).

[48] P. D. Maker and R. W. Terhune, Phys. Rev. **137**, A801 (1965).

[49] A. Nahata and T. F. Heinz, Opt. Lett. **23**, 67 (1998).

[50] D. Cook, J. Chen, E. Morlino, and R. Hochstrasser, Chem. Phys. Lett. **309**, 221 (1999).

[51] Z. Mics, K.-J. Tielrooij, K. Parvez, S. A. Jensen, I. Ivanov, X. Feng, K. Müllen, M. Bonn, and D. Turchinovich, Nat. Commun. **6**, 7655 (2015).